ARTICLE

Microheater Integrated Nanotube Array Gas Sensor for Parts-Per-Trillion Level Gas Detection and Single Sensor-Based Gas Discrimination

Wenying Tang,[§] Zhesi Chen,[§] Zhilong Song, Chen Wang, Zhu'an Wan, Chak Lam Jonathan Chan, Zhuo Chen, Wenhao Ye, and Zhiyong Fan*

ACCESS | Metrics & More | Article Recommendations | Supporting Information

ABSTRACT: Real-time monitoring of health threatening gases for chemical safety and human health protection requires detection and discrimination of trace gases with proper gas sensors. In many applications, costly, bulky, and power-hungry devices, normally employing optical gas sensors and electrochemical gas sensors, are used for this purpose. Using a single miniature low-power semiconductor gas sensor to achieve this goal is hardly possible, mostly due to its selectivity issue. Herein, we report a dual-mode microheater integrated nanotube array gas sensor (MINA sensor). The MINA sensor can detect hydrogen, acetone, toluene, and formaldehyde with the lowest measured limits of detection (LODs) as 40 parts-per-trillion (ppt) and the theoretical LODs of ∼7 ppt, under the continuous heating (CH) mode, owing to the nanotubular architecture with large sensing area and excellent surface catalytic activity. Intriguingly, unlike the conventional electronic noses that use arrays of gas sensors for gas discrimination, we discovered that when driven by the pulse heating (PH) mode, a single MINA sensor possesses discrimination capability of multiple gases through a transient feature extraction method. These above features of our MINA sensors make them highly attractive for distributed low-power sensor networks and battery-powered mobile sensing systems for chemical/environmental safety and healthcare applications.

KEYWORDS: gas sensor, pulse-heating, trace gas detection, machine learning algorithm, single-sensor gas discrimination
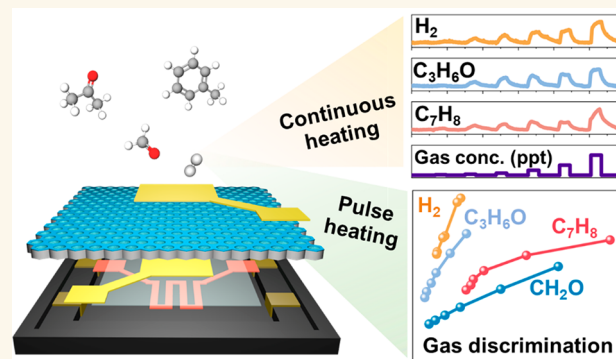
INTRODUCTION

Detection of various life threatening gaseous molecules is of paramount importance in many fields including environmental monitoring, food quality evaluation, industrial safety, explosive detection, healthcare, *etc*.[1−8] Conventionally, costly, bulky, and power-hungry devices, mostly employing optical gas sensors and electrochemical gas sensors, are used for this purpose. In fact, metal oxide (MOX) semiconductor gas sensors possess a number of alluring attributes such as low cost, small formfactor, reasonable lifetime, and excellent compatibility with other electronic components. Thus, in principle, they are the ideal candidates for highly integrated sensor systems.[9−19] However, poor selectivity and sensitivity of the mainstream MOX sensors have been the main roadblocks hindering their wide applications. Meanwhile, the high operating temperature (300−400 °C) also limits the employment of MOX-based gas

sensors in portable electronics due to high power consumption.[15]

Recently, researchers have devoted great efforts to overcome the drawbacks of MOX-based gas sensors. Various strategies, such as adding a porous overlayer above the sensor films as molecular sieve, or functionalizing the surface with noble metals or oxides as catalytic sites, have been adopted to improve the poor selectivity and LOD of the MOX-based gas sensors.[20−22] Gas sensor arrays integrated with multiple gas sensors have also been demonstrated as an effective method to
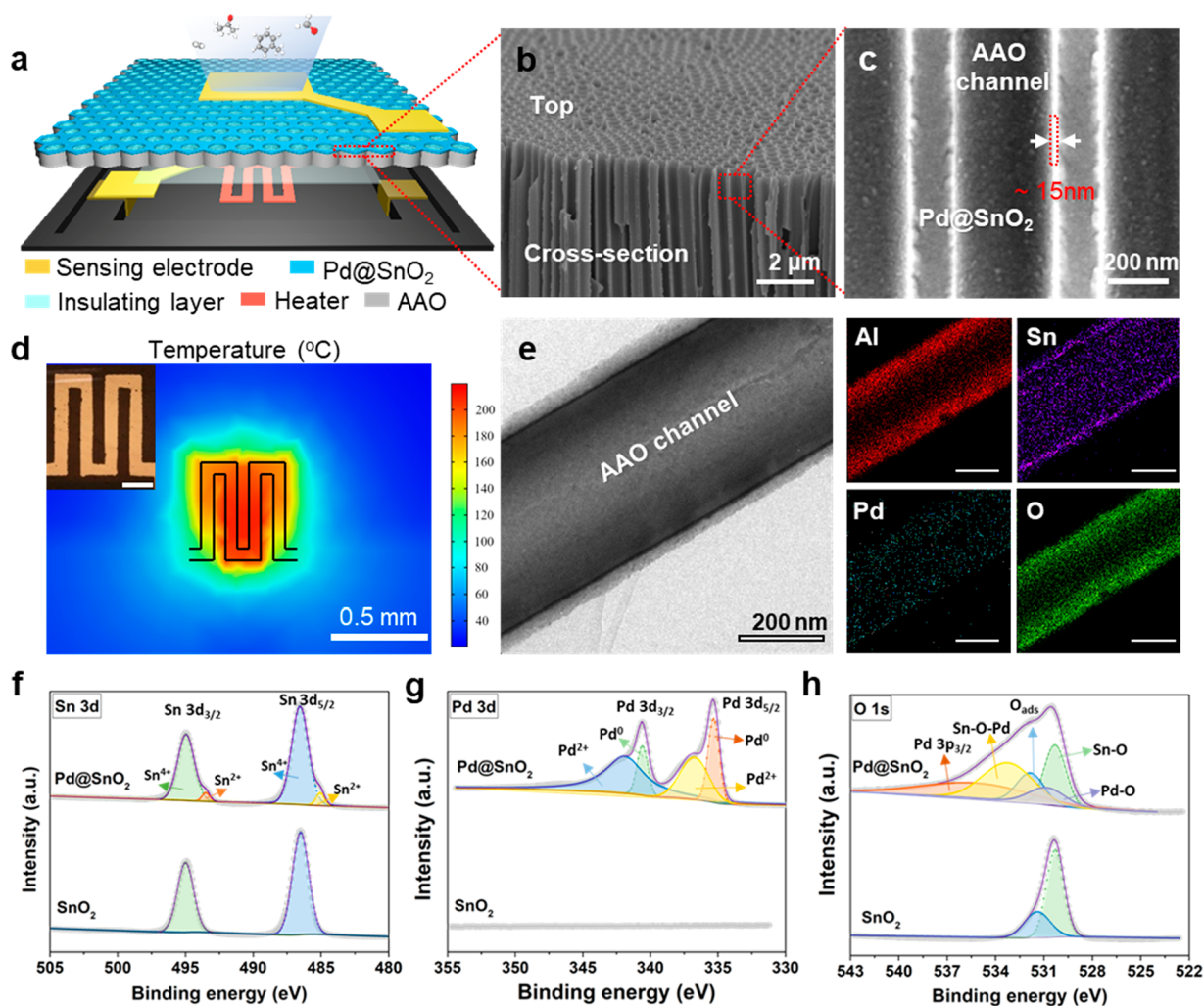
Figure 1. Schematic and characterization. (a) Schematic diagram of MINA sensor. (b, c) SEM images of Pd@SnO₂ nanoparticles: (b) overview and (c) cross-section. (d) Thermal simulation of microheater under 40 mW heating by COMSOL, insert figure is the actual heater image under optical microscope with scale bar of 0.2 mm. (e) TEM image of Pd@SnO₂ and elements mapping. (f–h) XPS spectrums of SnO₂ and Pd@SnO₂. High-resolution spectra of (f) Sn 3d, (g) Pd 3d, and (h) O 1s.

discriminate multiple gases, attributing to their abundant extractable output information.[23−25] However, complicated sensor array construction and data processing are still inevitable, and implementing the gas discrimination with single sensor is in urgent pursuance. One option is to add a molecular sieve in front of a single sensor, which discriminates gases by time-series data depending on gas diffusion properties in the molecular sieve.[26] However, the molecular sieve needs to be replaced frequently to avoid contamination and it is difficult to detect trace molecules because of strong adsorption of the target molecules on the molecular sieve. Alternatively, dielectric excitation measurements have been applied to gas discrimination using individual sensor via frequency-dependent multivariable response.[27] However, its complexity of data acquisition and interpretation hinders its application from real-time gas discrimination. In comparison, temperature modulation, which is more preferable due to its ease of operation, has been broadly utilized to extract temperature-related kinetic information.[28−32] Nonetheless, most of the relative studies discriminated gas species according to the sensor response variations at different temperatures by applying CH mode, which has difficulty in realizing real-time gas species recognition due to the long operation periods. Pulse heating,

featuring periodic transient thermal cycle, has great potential on real-time gas discrimination since it can provide the transient characteristics of multivariable response emerging from gas diffusion and gas−solid surface reactions between gas molecules and sensing materials.[33−37] However, most of the proposed pulse-driven MOX sensors focused on reducing power consumption and improving gas sensing performance including sensitivity and fast recovery ability. The gas discrimination ability of pulse-driven MOX sensors through extracting transient features has been rarely explored in the past.

Herein, we demonstrate a dual-mode microheater integrated nanotube array gas sensor (MINA sensor) that can detect multiple gases down to ppt level under CH mode and discriminate the gases when working under PH mode. A MINA sensor was built on nanoporous anodic aluminum oxide (AAO) templates with top-bottom electrodes structure to enable much enhanced surface area for the molecular access. The ultrathin and conformal SnO₂ thin film and Pd nanoparticles (NPs) were deposited by atomic layer deposition (ALD) as the sensing material layer. When being operated under CH mode, the MINA sensor can detect hydrogen, acetone, toluene, and formaldehyde with measured LODs as

low as 40 ppt, 40 ppt, 40 ppt, and 4 ppb, with the corresponding theoretical LODs of 6.96 ppt, 11.88 ppt, 16.52 ppt, and 70.06 ppt, respectively. Under PH mode, the MINA sensor shows intriguing transient responses toward different gases because of the variations of gas diffusion and activation energy of surface reactions. Gases of hydrogen, acetone, toluene, and formaldehyde have been distinguished by extracting conductance and slope features from each pulse. Moreover, the pulse heating mode saves 66.7% energy compared with traditional continuous heating mode. The ppt level gas detection and pulse-heating enabled gas discrimination by a single MINA sensor exhibit promising potential for high-performance, low-power, and miniature smart gas sensors for sensor networks and mobile/wearable electronic applications.

RESULTS AND DISCUSSION

MINA Sensor Fabrication and Characterization. Figure 1a illustrates the schematic diagram of our MINA sensor, which was fabricated on a nanoporous AAO template with a three-dimensional top-bottom electrode configuration. In this structure, the top electrode is a simple electrode in contact with the sensing material. And at the bottom side, there are three layers, namely the bottom sensing electrode layer, the insulating SiO_2 layer, and the microheater layer. The fabrication process is detailed in Figure S1. Briefly, a conformal SnO_2 thin layer was first deposited into the channels of AAO by ALD (Methods) and annealed at 450 °C for 3.5 h to form the intrinsic SnO_2 (Figure S1a−c). Then Pd NPs with different thickness controlled by ALD cycles (x_{Pd}) were deposited on SnO_2 thin film (Figure S1d; Methods). These sensors are marked as x-Pd@SnO_2 (x = 10, 20, 30, 40) for simplicity. The cross-sectional view and element mapping of 20-Pd@SnO_2 clearly reveal the uniform decoration of Pd onto SnO_2 layer and the conformal coating of Pd@SnO_2 sensing layer onto AAO channels with average thickness of ∼15 nm (Figure 1b,c,e). The XRD patterns of pristine SnO_2 and Pd@SnO_2 (Figure S2) confirm the face-centered cubic and tetragonal rutile structures of Pd and SnO_2, respectively. After Pd@SnO_2 sensing layer deposition, the top Au electrode was deposited (Figure S1e), and the AAO was flipped over and bottom sensing electrode was aligned with the top electrode and deposited (Figure S1f). Thereafter, a patterned SiO_2 insulating layer was deposited on the bottom sensing electrode (Figure S1g),to prevent the current leakage issue between bottom sensing electrode and heater. Then Pt microheater was evaporated on the insulating layer (Figure S1h). The microheater size is ∼600 × 600 μm^2. Thus, the functional area of the sensor is confined to 0.36 mm^2, as shown in Figures 1d and S3a. Here, all the sensing electrodes, insulating layer, and microheater layer were evaporated with photolithography-free methods, which were facile and low-cost. It is important to mention that the conventional microheater powered gas sensors are all fabricated on silicon (Si) substrates.[38−44] Because of high thermal conductivity of Si (k = 148 W/(m*K)), the microheaters must be fabricated into much smaller size (*e.g.*, 150 × 150 μm^2) as compared to our microheater.[38] And the supporting Si under the microheaters must be etched to ∼2.5 μm thick with photolithography patterning followed by precisely controlled wet or dry etching to reduce lateral heat dissipation and maintain the heater temperature.[38−44] However, intriguingly, the constituent material of AAO, that is, alumina, has much lower thermal

conductivity (k = 1.38 W/m K).[45] Moreover, the honeycomb-like nanotube structures of AAO template further reduce horizontal heat conduction, leading to confined heating zone for the MINA sensor, as confirmed by COMSOL simulation (Figures 1d and S3b; Methods). The combination of these two factors led to excellent heat utilization efficiency of the microheater on AAO. The temperature−power curve and temperature−voltage curve of the deposited heater were measured and are shown in Figure S3c and d. The MINA sensor features ultralow heating power density (0.111 $\mu W/\mu m^2$ at 200 °C). This is on a par with that in commercial MOX gas sensors on Si that are fabricated with sophisticated processes as mentioned (Table S1).

To examine the effects of Pd NPs coated on SnO_2 surface, X-ray photoelectron spectroscopy (XPS) was carried out (Figure 1f−h). In Sn 3d spectra, both pure SnO_2 and Pd@SnO_2 samples have Sn^{4+} $3d_{3/2}$ (495 eV) and Sn^{4+} $3d_{5/2}$ (486.5 eV) peaks, while Pd@SnO_2 has extra Sn^{2+} peaks (485.1 and 493.5 eV), which are attributed to surface segregation of doping-ions leading to the reduction of Sn^{4+} into Sn^{2+}. (Figure 1f).[46,47] According to Pd 3d spectra, 68.2% of Pd molecules are oxidized to Pd^{2+}, while the rest remain to be Pd^0 (Figure 1g).[48] The asymmetric O 1s spectra of pure SnO_2 sample can be separated into a SnO_2 lattice oxygen peak (530.3 eV) and a chemisorbed oxygen peak (531.4 eV). Spectra of Pd@SnO_2 have five peaks, namely SnO_2 lattice oxygen peak (530.3 eV), PdO lattice oxygen peak (530.8 eV), chemisorbed oxygen peak (531.9 eV), coordinated oxygen in Sn−O−Pd (533.3 eV), and a mixed Pd $3P_{3/2}$ peak (535.2 eV) (Figure 1h).[48,49] The asymmetric O 1s spectra of the two samples proves that the addition of Pd NPs increases the quantity of adsorbed oxygen species, which is an essential factor to improve our sensor performance.

Trace Gas Detection and Gas Discrimination under CH Mode. A MINA sensor was bonded to a chip-carrier for operating temperature control and sensing signal readout (Figure S1i). Sensing performance of x-Pd@SnO_2 MINA sensors was first evaluated under CH mode to explore the optimal fabrication and operating conditions by adopting a series of heating power from 20 to 80 mW (∼120 to 350 °C), and 50 ppb hydrogen was used as a reference (Figure S4). Gas response here is defined as *Response* (%) = (G_a/G_g−1) × 100, where G_a and G_g are the conductance in air and target gas, respectively. As shown in Figure S4, with the increasing of heating power, all the x-Pd@SnO_2 MINA sensors first show improved response toward 50 ppb hydrogen; however, when heating power exceeds 40 mW (∼200 °C), the response degrades. This can be attributed to the temperature (T_{op})-dependent surface chemical reaction (SCR) and target gas diffusion.[50] When T_{op} < 200 °C, SCR limits the process, so sensing response increases with the elevation of temperature, attributing to enhanced reactivity between gas molecules and Pd@SnO_2. However, when T_{op} exceeds 200 °C, the gas−solid reaction becomes gas-diffusion-limited, and the higher the T_{op}, the more difficult for gas molecules to diffuse into Pd@SnO_2 thin-film for sensing reactions; thus, higher temperature leads to the decreased response when T_{op} > 200 °C. It is reported that Pd loading on pristine SnO_2 can improve the sensing performance due to the noble metal catalytic effect, which enlarges the quantity of adsorbed oxygen species proved by O 1s XPS spectra and accelerates the gas sensing-related surface reactions.[51] Thus, the effects of Pd thickness were also studied by precisely controlling the number of ALD cycles to fabricate
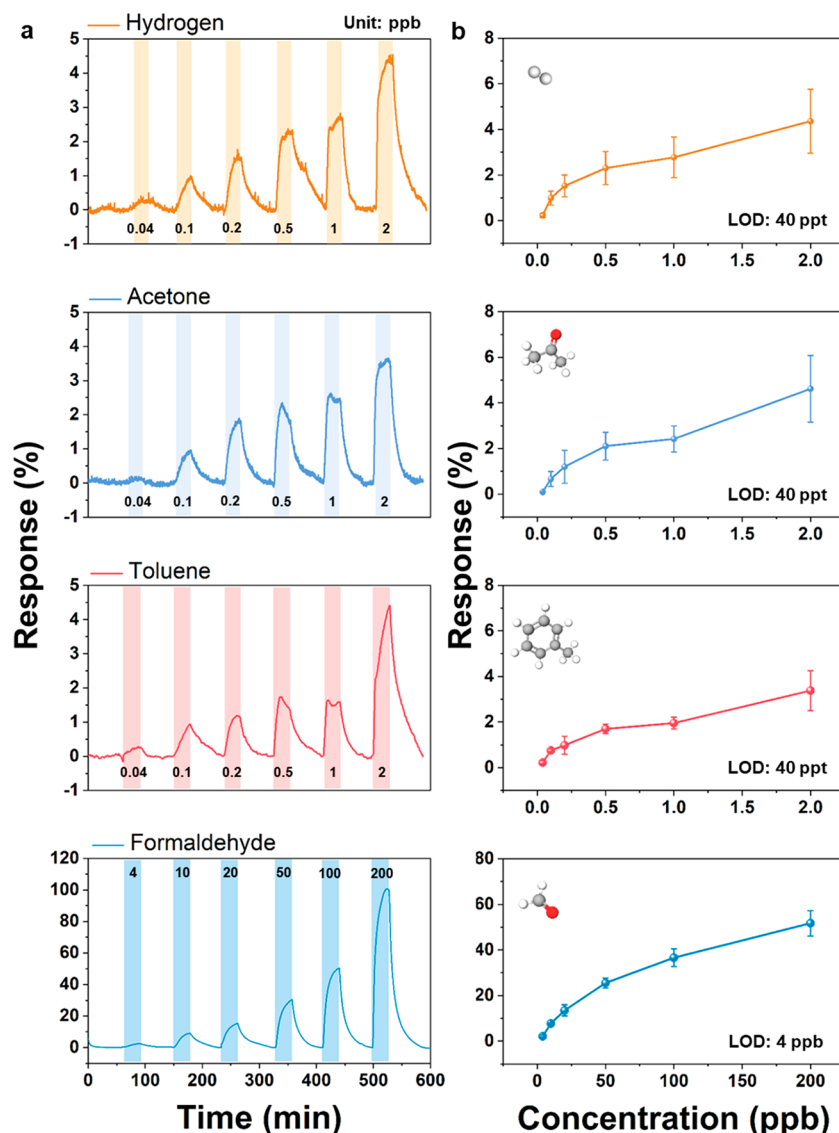
Figure 2. Trace-gas sensing measurement under CH mode (40 mW). (a) Transient curves of ultralow concentration gas sensing performance toward 0.04−2 ppb hydrogen, 0.04−2 ppb acetone, 0.04−2 ppb toluene, and 4−200 ppb formaldehyde. (b) Response versus concentration curves toward hydrogen, acetone, toluene, and formaldehyde.

the x-Pd@SnO$_2$ MINA sensors (x = 10, 20, 30, 40). When being operated under the same heating power, response of x-Pd@SnO$_2$ MINA sensors toward 50 ppb hydrogen first increases with thicker Pd decoration and decreases when ALD cycles are more than 20 cycles. The variation in MINA sensor performance induced by the amount of Pd can be explained by the competition between the number of available active adsorption sites on SnO$_2$ surface and the surface catalytic activity. When $x_{Pd} \leq 20$, more Pd loading on SnO$_2$ helps to adsorb more oxygen molecules and activate the dissociation of more reducing gas molecules, resulting in higher gas response. However, when the Pd loading is excessively high ($x_{Pd} > 20$), it occupies too many available active sites on SnO$_2$ surface for oxygen and target gases adsorptions; thus, the sensing process is hindered.

Since 20-Pd@SnO$_2$ MINA sensor under 40 mW (∼200 °C) has the highest response, it is selected for further evaluation of trace gas detection ability. Hydrogen, acetone, toluene (from 40 ppt to 2 ppb), and formaldehyde (from 4 to 200 ppb) were separately introduced to the MINA sensor for the evaluation

(Figure 2). The 20-Pd@SnO$_2$ MINA sensor shows obvious sensing signals toward the injected four gases (Figure 2a), and the corresponding response values are extracted and plotted in Figure 2b. The measured LODs are 40 ppt for hydrogen, acetone, and toluene with corresponding response values of 0.230%, 0.093%, and 0.219%, and their theoretical LODs are as low as 6.96 ppt, 11.88 ppt, and 16.52 ppt, respectively (Figure S5a−c; Methods). For formaldehyde, the measured LOD is 4 ppb with the response of 2.18%, and the theoretical LOD is calculated to be 70.06 ppt (Figure S5d; Methods). The optimal MINA sensor is demonstrated to have the lowest measured LODs toward hydrogen, acetone, toluene, and formaldehyde compared with the reported MOX-based gas sensors (Tables S2−S5). The excellent ppt level gas detection ability of MINA sensor can be attributed to the large sensing surface and the great surface catalytic activity of Pd decoration under the optimal operating temperature.

Although our MINA sensors have great potential for ppt level gas detection, the response values toward different gases with the same concentrations are similar (Figure S6). Inspired
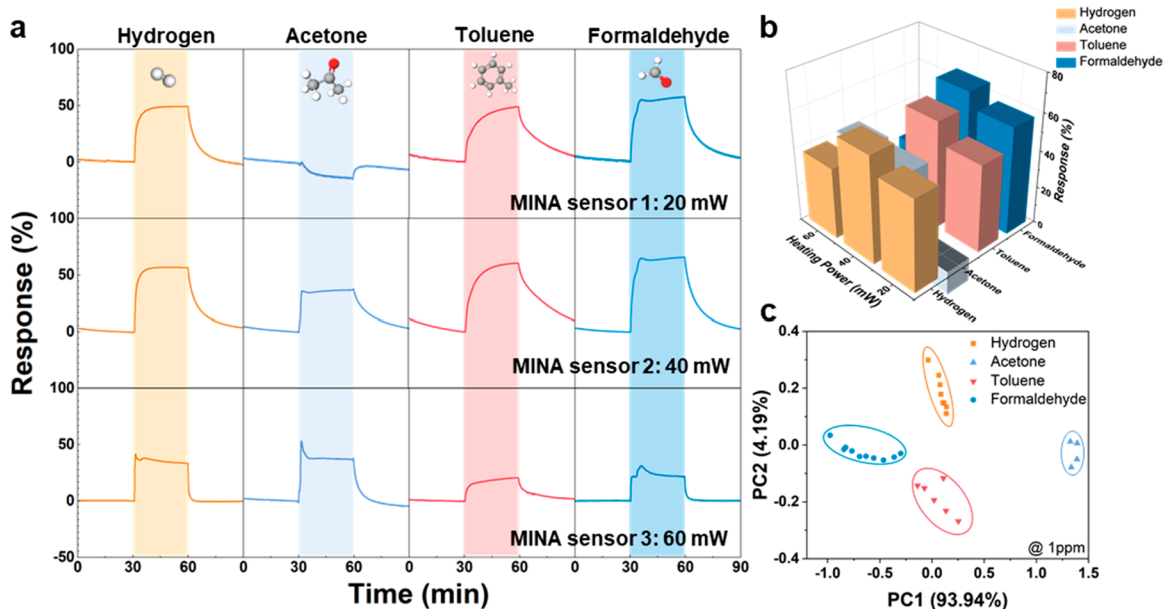
Figure 3. Gas discrimination with CH modes. (a) Response−time curve for MINA sensor array operated under 20, 40, and 60 mW CH modes when exposed to 1 ppm hydrogen, acetone, toluene, and formaldehyde. (b) 3D bar chart of response values with respect to the mentioned target gases as a function of heating power. (c) PCA gas discrimination result of the mentioned target gases.

by temperature-dependent sensing behaviors analyzed above, a MINA sensor array consists of three identical 20-Pd@SnO$_2$ MINA sensors operated under 20, 40, 60 mW (∼120, 200, 280 °C) was constructed for gas discrimination, each being a good representative of the sensing process under SCR-limited mode, SCR-diffusion balance mode, and diffusion-limited mode, respectively. One ppm hydrogen, acetone, toluene, and formaldehyde were separately introduced to MINA sensor array to explore its discrimination capability. When exposed to the same gas, these identical MINA sensors have different sensing behaviors under 20, 40, 60 mW heating, especially the response value and response time (Figures 3a,b and S7b,c). Here, response time (t_{res}) is defined as the time required by MINA sensor to reach 90% of the saturated response in the target gas atmosphere (Figure S7a).[52]

The differences of the response patterns generated by different operating temperatures can be attributed to the competitions between surface reactivity and gas molecule diffusions, as analyzed in the previous part. Most of the response values are positive, which means MINA sensors' conductance increases with the injections of the target gases. It is due to the oxidation of the four reducing gases that releases free electrons to the conducting channels.[53] Interestingly, the response value toward 1 ppm acetone is negative, when MINA sensor is operated under 20 mW (Figure 3a,b). This is because under 20 mW (∼120 °C), the chemisorption and chemical reaction of acetone sensing process are marginal; thus, the adsorbent-induced variations of the mean free time (τ_n) of the conduction carriers dominate the change of the conductance under 20 mW heating. In other words, physical-adsorbed acetone molecules alter τ_n by serving as scattering centers, which decrease the conductance of 20 mW-heating MINA sensor.[54−56] In terms of response time, it decreases as operating temperature increases (Figure S7b). This is because higher operating temperature leads to higher rate constant of surface reaction between target gases and adsorbed oxygen, resulting in faster changes of MINA sensor's conductance.

As illustrated in Figure 3c, we have successfully achieved the discrimination of four gases by principal component analysis (PCA), taking advantages of the response patterns generated by the above-mentioned 3-pixel power-varying MINA sensor array with the saturated sensing responses as inputs. The points representing each gas aggregate in a circled cluster with obvious separation among each gas, which further prove the good gas discrimination ability of MINA sensor array. Moreover, we compare gas discrimination results from 3-pixel MINA sensor array and 4-pixel MINA sensor array, the latter with an extra pixel under 80 mW, and find them resembling each other, as evident from Figures 3c and S7d. From a mathematical perspective, PCA is one of the dimensionality-reduction algorithms, achieving dimensional reduction and removing the redundancy by creating principal orthogonal vectors with maximized variance among the input dataset.[57] The distributions of response points show high similarity between the discrimination results of 3-pixel MINA sensor array and 4-pixel MINA sensor array, confirming that most of the information (variation of response patterns) regarding the interaction of gases and MINA sensor array arises from three heating power values, 20, 40, and 60 mW. It must be mentioned that 80 mW does not provide extra information as it represents the same sensing mode (diffusion-limited mode) as 60 mW one and can be considered as redundant.

Single Sensor-Based Gas Discrimination under PH Mode. Inspired by the dynamics of gas−solid interaction triggered by the thermal activation, a pulse-driven heating voltage (V_H) is applied to the microheater for heating temperature adjustment. Intriguingly, we have discovered that the multivariable features extracted from one single sensor under this PH working mode enable gas discrimination with one single sensor. In this scenario, pulse-on (2 V, 10 s) and pulse-off (0 V, 20 s) cycles were periodically repeated during the whole gas sensing measuring processes. Note that the pulse-on voltage leads to 200 °C heater temperature (Figure S3d). Dynamic sensing transients of PH-mode-driven MINA
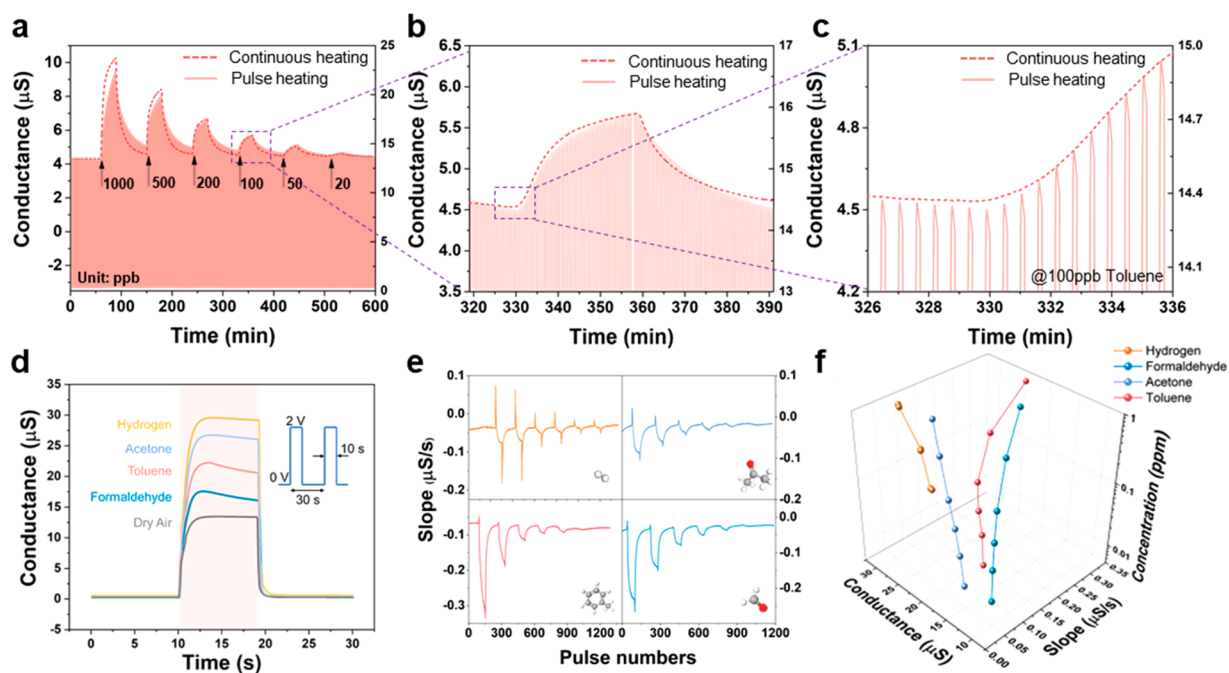
Figure 4. Gas sensing properties under PH mode. (a) Pulse heating and continuous heating transient curves toward 1000, 500, 200, 100, 50, 20 ppb toluene, (b) zoom-in curves toward 100 ppb toluene, (c) zoom-in curves at the beginning of introduction of 100 ppb toluene (left axis, CH mode; right axis, PH mode). (d) Transient curves under single pulse toward 1 ppm hydrogen, acetone, toluene, formaldehyde and dry air. (e) Slope extractions versus pulse numbers toward hydrogen (1000, 1000, 500, 500, 200, 200 ppb), acetone (1000, 500, 200, 100, 50, 20 ppb), toluene (1000, 500, 200, 100, 50, 20 ppb), and formaldehyde (1000, 500, 200, 100, 50, 20 ppb). (f) 3D plot of conductance versus slope diagram for gas discrimination.
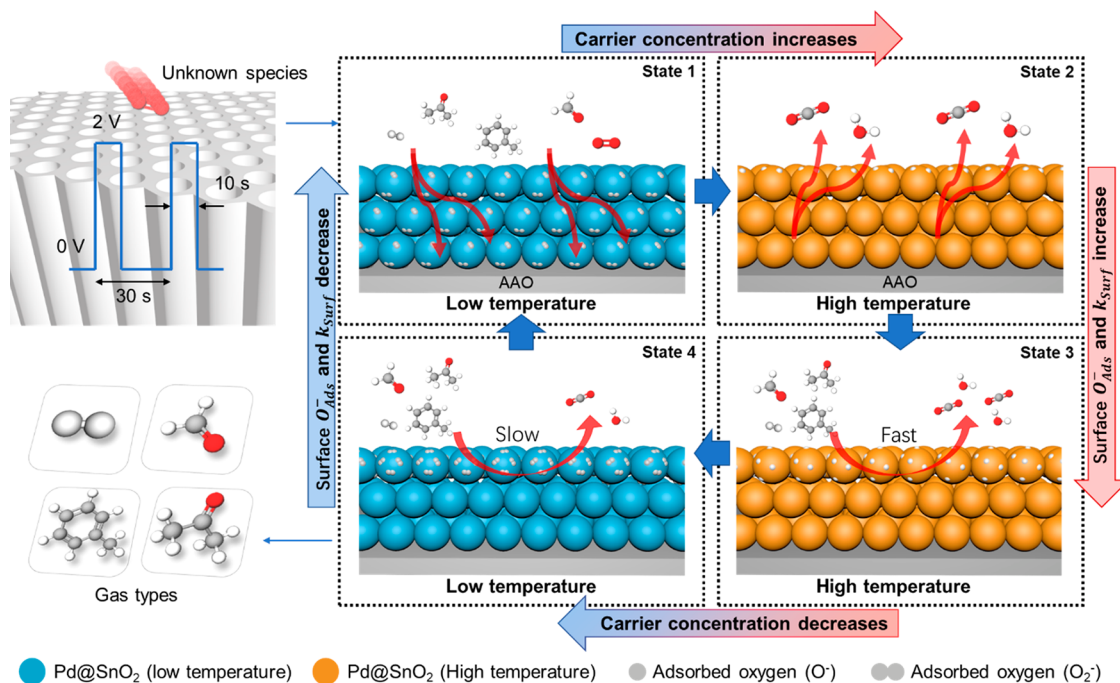

Figure 5. Schematic diagram of gas sensing behaviors under PH mode. O_{ads}^- and k_{surf} in the figure represent surface adsorbed oxygen and surface reaction rate, respectively.

sensor toward different concentrations of hydrogen, acetone, toluene, and formaldehyde were measured. Consisting of numerous single pulses, dynamic sensing curves of PH-mode-driven MINA sensor have consistent shapes with the CH-mode-triggered counterpart (Figures 4a−c and S8). This is because the sensing behaviors of MINA sensor under high

temperature of both CH mode and PH mode are similar, where the sensor conductance increases due to the consumption of surface adsorbed oxygen attributed to redox reactions with target gases. Interestingly, more transient features can be extracted from single pulses. As plotted in Figure 4d, when pulse voltage is turned on, conductance of

MINA sensor abruptly jumps from several hundred nS to several μS. After reaching its maximum, conductance of MINA sensor slowly decreases and jumps back to original level right after pulse voltage is turned off. It is worth mentioning that during the pulse-on phase (pink area in Figure 4d), the magnitude of conductance and its transient behavior vary with gas species. For the conductance magnitude variations during the pulse-on phase, MINA sensor exposed to 1 ppm hydrogen environment shows the biggest change, followed by acetone, toluene, and formaldehyde, as shown in Figure 4d. To examine transient behavior of conductance during the pulse-on phase, a five-second-long conductance curve was extracted from the curve (Figure S9a,b), whose slope was extracted after fitting the curve with a linear formula by the least-squares methods (Figure S9c). For 1 ppm hydrogen, acetone, toluene, and formaldehyde, the slope values are −0.0784, −0.086, −0.325, and −0.230, respectively. Slopes have similar dynamic transients versus pulse numbers as conductance versus time plots, and the overshooting of slopes, which is caused by the nonequilibrium target gas distribution, reveals the processes of target gas injection and removal (Figures 4e and S10). Interestingly, the conductance magnitudes and the transient slopes during pulse-on phase have negative correlations. The reasons can be explained with gas diffusion models and surface gas–solid reaction models (Mechanism Analysis). In short, transient conductance curves during pulse-on phase contain information about gas diffusion and surface gas–solid reaction, which varies with gas species and can be utilized for gas discrimination. Therefore, by creating a pulse-on 3D conductance–slope (C−S) diagram, where the slopes are extracted from the stable target gas distribution period, hydrogen, acetone, toluene, and formaldehyde with different concentrations can be discriminated (Figure 4f). Moreover, the C−S diagram shows clear directionality with the increment of concentration of identical gas, which reveals its excellent discriminability toward the tested four gases.

Mechanism Analysis. According to previous reports on pulse heated gas sensors, during one pulse heating cycle, a sensor undergoes transition among four states: low-temperature equilibrium state (state 1), high-temperature nonequilibrium state (state 2), high-temperature equilibrium state (state 3), and low-temperature nonequilibrium state (state 4), as shown in Figure 5.[58−60] For our MINA sensor, target gases molecules diffuse and condense on the sensing layer during pulse-off phase (low temperature, state 1, 4) and react with adsorbed oxygen molecules during pulse-on phase (high temperature, state 2, 3).[32,34,35] After the temperature switch, a new equilibrium needs to be established, and the relaxation from nonequilibrium state to equilibrium state highly depends on the gas species in the ambient.[58−60]

As discussed in the last section, the conductance change magnitude and slope during the transition from state 2 to 3 vary with gas species (Figure 4d), which reveal the varied relaxation behaviors in different gaseous environment. Here, we further explore the relaxation behaviors through gas diffusion theory and Eley−Rideal model.[61−64] First, gas-diffusion theory is briefly introduced.[61] MOX gas sensor's responses are determined by two parameters, rate constant k and diffusion coefficient D_k. Here, Knudsen diffusion is utilized to describe the gas diffusion in Pd@SnO$_2$ sensing layer since the pores between Pd@SnO$_2$ sensing particles have average radius as 10−20 nm (Figure 1c).[61] For rate constant k, the mathematic expression is

$$k = k_0 \exp\left(-\frac{E_a}{RT}\right) \tag{1}$$

where E_a and k_0 are activation energy of the first-order reaction and pre-exponential constant, respectively. R is gas constant and T is temperature. And for Knudsen diffusion coefficient D_k, the mathematic expression is

$$D_k = \frac{4r}{3}\sqrt{\frac{2RT}{\pi M}} \tag{2}$$

where r, T, and M are pore radius, temperature, and gas molecular mass, respectively.

Under the same temperature, k is controlled by E_a, and D_k is controlled by M. According to literatures, the variations of conductance magnitude from state 2 to 3 can be attributed to different diffusion depths of the four gases caused by the variation of E_a and D_k.[32,61,65] In fact, the values of E_a of the combustion reaction between surface adsorbed oxygen molecules and target gas molecules have been calculated based on the Eley−Rideal model.[62−64] Conductance change is directly correlated with surface oxygen coverage, and it can reflect gas interaction processes. When our MINA sensor is working under the continuous heating mode, admittance of target gas molecules into the test chamber results in transient responses of the sensor conductance (Figure S11a). Particularly, the transient curve can be fitted with exponential equations as

$$G(t) = G_0 + G \exp\left(-\frac{t}{\tau_{res/rec}}\right) \tag{3}$$

where $G(t)$ is the time-dependent conductance, G_0 and G are the fitting constants, and $\tau_{res/rec}$ is relaxation time constant for response/recovery processes (Figure S11a).[64] Here, only response time constant needs to be considered since gas molecule adsorption and combustion reaction with surface oxygen can already be used to determine the value of E_a.

According to the temperature-dependent gas sensing kinetics, response constant (τ_{res}) can be simplified and expressed as

$$\tau_{res} = \nu^{-1} \exp\left(\frac{E_a}{2KT}\right) \tag{4}$$

where ν is frequency-relative constant, E_a is the activation energy for combustion reaction, K is the Boltzmann constant, and T is the operating temperature in Kelvin.[64,66,67]

Transient curves of MINA sensor toward 1 ppm hydrogen, acetone, toluene, and formaldehyde under continuous 20, 40, 60, 80 mW heating (∼120, 200, 280, 350 °C) are used for τ_{res} extraction. By plotting $\ln(\tau_{res})$ versus $1/2KT$, activation energy of hydrogen, acetone, toluene, and formaldehyde can be calculated as 0.460 eV, 0.452 eV, 0.470 and 0.243 eV, respectively (Figure S11b). Thus, these four gases are ranked with activation energy from lowest to highest as formaldehyde, acetone, hydrogen, and toluene. The gas with the smallest activation energy is consumed the most under low temperature since it requires the least energy to trigger the combustion reaction.

From eq 2, D_k is controlled by M only, and T and r are the same for each case since the gas sensing measurement was conducted with identical MINA sensors. The larger M, the smaller D_k, under the same temperature. Thus, these four gases

are ranked with diffusion constant values from highest to lowest as hydrogen, formaldehyde, acetone, and toluene.

Hydrogen, acetone, and toluene have similar activation energy values, which means that their diffusion depths during pulse-off phase are determined by their diffusion abilities. Since hydrogen has the highest D_k, extra hydrogen molecules can diffuse the most deeply into Pd@SnO$_2$ sensing layer during pulse-off phase, followed by acetone and toluene (Figure S12c). For formaldehyde, as discussed above, it has the lowest activation energy among these four gases, which means its combustion reaction can happen under lower operating temperature than the others. Thus, not as many formaldehyde molecules as the rest of gases can diffuse into Pd@SnO$_2$ sensing layers during pulse-off phase, depicting the thinnest depletion layer in Figure S12c. When V_H switches from 0 to 2 V, the extra gas molecules that diffuse into Pd@SnO$_2$ sensing layer are combusted, as shown in Figure S12d. The combustion reactions consume the adsorbed oxygen species in the deep sensing layer, returning the trapped electrons to conducting channels and leading to the increase of conductance. Since hydrogen diffuses the deepest into the sensing layer, it induces the largest conductance magnitude change during one temperature cycle, followed by acetone, toluene, and formaldehyde (Figure 4d).

The variations of conductance transient trends from state 2 to 3 can be directly explained by the difference of oxygen readsorption quantity, which depends on the surface reaction rate. The faster the surface reaction rate, the more oxygen is consumed, the smaller the quantity that oxygen can be readsorbed. Here, according to the surface gas sensing kinetic model, response time constant expression can be changed into:

$$\tau_{res} = (k_r C_V + k_{-r})^{-1}$$

where k_r is the surface combustion reaction constant, C_V is concentration of reducing gas, and k_{-r} is inverse kinetic reaction rate constant.[64,67,68]

Here, transient curves of MINA sensor toward 1000/500/200/100/50 ppb hydrogen, acetone, toluene, and formaldehyde under 40 mW (~200 °C) are used for τ_{res} extraction. By plotting $1/\tau_{res}$ versus C_V curve, surface reaction constant k_r can be extracted. The values of k_r for hydrogen, acetone, toluene, and formaldehyde are 7.32 e^{-6}, 6.42 e^{-6}, 3.02 e^{-6}, and 2.57 e^{-6}, respectively (Figure S11c). Thus, for hydrogen, which has the highest surface combustion reaction constant under 40 mW (~200 °C), it consumes oxygen so fast that oxygen from ambient environment can only supply to near-surface layer, leading to the smallest conductance change between state 2 to 3. Similar explanations can be applied to acetone. For toluene and formaldehyde, their oxygen consumptions are located near surface of sensing layer, and their k_r values are smaller than hydrogen and acetone, which means oxygen can be supplied quickly and results in higher oxygen occupation ratio than others. Thus, toluene and formaldehyde have obvious conductance changes between state 2 to 3.

CONCLUSIONS

Herein, a dual-mode MINA sensor has been developed, demonstrating capability of detecting ppt level gases and recognizing them by using one single sensor. The device has a three-dimensional architecture mainly consisting of Pd coated SnO$_2$ nanotubes with ultrahigh surface-to-volume ratio, and an integrated high efficiency microheater. When the device was operated under CH mode, we have measured the record low LODs with MINA sensors toward hydrogen (LOD = 40 ppt), acetone (LOD = 40 ppt), toluene (LOD = 40 ppt), and formaldehyde (LOD = 4 ppb), with their theoretical LODs of 6.96 ppt, 11.88 ppt, 16.52 ppt, and 70.06 ppt. Furthermore, single MINA sensor demonstrated excellent gas discrimination capability when it was operated under PH mode, enabled by extraction of characteristic diffusion and reaction kinetics during operation. These above features of our MINA sensors make them highly attractive for distributed low-power sensor networks and battery-powered mobile sensing systems for chemical/environmental safety and healthcare applications.

METHODS

SnO$_2$ and Pd ALD. A 15 nm-thick uniform SnO$_2$ thin film was deposited into AAO channels by ALD (MNT Micro and Nanotech Co., Ltd.) with cycle numbers of 45, where Tetrakis (dimethylamino) tin (C$_8$H$_{24}$N$_4$Sn, TDMAS, 99.999%) and deionized H$_2$O were injected into the reactor (150 °C) alternatively with N$_2$ as the carrying and purging gas. The injecting sequence was "TDMAS (500 ms pulse, 5 s waiting) − N$_2$ (30 s purging) − H$_2$O (50 ms pulse, 5 s waiting) − N$_2$ (30 s purging)". Next, Pd NPs were also deposited by the ALD method with cycles of 10, 20, 30, and 40. Reactor temperature for Pd ALD was 200 °C, precursors were Palladium(II) hexafluoroacetylacetonate (99.999%) and hydrazine anhydrous, and N$_2$ was the carrying and purging gas. The injecting sequence was "Palladium(II) hexafluoroacetylacetonate (1000 ms pulse, 5 s waiting) − N$_2$ (30 s purging) − hydrazine anhydrous (200 ms pulse, 5 s waiting) − N$_2$ (30 s purging)".

Sensing Electrodes, Insulating Layer, and Heater Evaporation. Metal shadow masks were utilized for sensing electrodes, insulating layer, and microheater layer evaporation. Fifteen nanometer titanium (Ti) and 150 nm gold (Au) were deposited in sequence onto each side of AAO with good alignment by thermal evaporation as vertical sensing electrodes. Then 1.5 μm SiO$_2$ was deposited on the bottom sensing electrode by e-beam evaporation as the insulating layer. Finally, 20 nm Ti and 180 nm platinum (Pt) were evaporated in sequence on the insulating layer by e-beam evaporation (IVS EB-500M, Innovative Vacuum Solution Co., Ltd.) to serve as the microheater.

Characterization. Morphology of MINA sensor was characterized by scanning electron microscope (SEM, JSM-7100F, JEOL) and high-resolution transmission electron microscope (HR-TEM, JEM 2010F, JEOL). EDS mapping was achieved by high-resolution transmission electron microscope (HR-TEM, JEM 2010F, JEOL). Element characterization was done by X-ray diffraction (XRD, X'pert Pro (PANalytical)) with scanning angle from 10−80°. XPS analysis was conducted to characterize chemical states of SnO$_2$ and Pd@SnO$_2$ samples for sensing performance analysis (XPS, Physical Electronics 5600 multitechnique system, Physical Electronics, Inc. (PHI)).

COMSOL Simulation. Temperature distribution of microheater on AAO was simulated by COMSOL Multiphysics 5.4a. The simulation model contained three Physics, namely electric current (EC), heat transfer in solids and fluids (HT), and surface-to-surface radiation (RAD). A device with the dimensions 800 × 800 × 50 μm^3 was modeled to simulate the temperature distribution. To simulate the real conditions and reduce computation power at the same time, Al$_2$O$_3$ with anisotropic thermal conductivity was assigned to AAO layer, where vertical thermal conductivity was set as 1.38 W/(m K), and horizontal thermal conductivity was set as 0.046 W/(m K). The microheater used platinum as the conducting material with 70 μm line width, 80 μm line gap, and 600 μm × 600 μm overall dimension.

For the EC part, electric potential of 2 V was applied to the microheater. The heat conducts from microheater to AAO via thermal conduction and radiation. The boundary conditions of AAO as hot plate and cold plate were set for convective heat flux. The heat transfer coefficient was calculated with the conditions of external natural convection and vertical wall. The surrounding environment

was set as atmosphere (1 atm, 70% humidity and 293.15 K). In RAD, the surface-to-surface radiation was applied to all the surfaces of devices.

Gas Sensing Measurement. Gas-sensing measurement was conducted with a homemade measurement system. Three mass flow controllers (MFC) (10, 500, and 500 sccm) were used, where MFC 1 and MFC 3 served as controllers for target gases injection, and MFC 2 flew compress air as carrying and diluting gas. After being mixed at a certain ratio, the diluted target gas was introduced into a homemade testing chamber, and the resistance signals were read out by Keithley 2400 (TEKTRONIX, INC.) as a function of time and processed by the home-built LABVIEW program. Power supply under CH mode was assisted by power source DP305B (Shenzhen Mestek Tools Co. LTD), whose power can be tuned by varying the voltage. For power supply under PH mode, another Keithley 2400 (TEKTRONIX, INC.) with a home-built C++ program was utilized to control the heating voltage. Pulse voltage was set as 2 V with pulse length of 10 s and reset to 0 V for 20 s.

LOD Calculations. Limit of detection (LOD) was calculated based on the standard deviation of the response (S_y) of the curve and the slope of the calibration curve (S). LOD was estimated according to the formula: LOD = $3 \times (S_y/S)$.[69]

ASSOCIATED CONTENT

ⓈⒾ Supporting Information

The Supporting Information is available free of charge at https://pubs.acs.org/doi/10.1021/acsnano.2c03372.

Fabrication flow of MINA sensor; X-ray diffraction result of SnO_2 and $Pd@SnO_2$ thin film; microheater morphology and thermal properties; MINA sensor optimization; theoretical LOD estimation results of MINA sensor; response comparison for 2−4 ppb H_2, acetone, toluene, and formaldehyde; additional sensing performance evaluation results; transient time-dependent sensing curves of MINA sensor to H_2, acetone, and formaldehyde under PH mode and CH mode; slope extraction method under PH mode; analysis for overshooting in slope versus pulse numbers plot during PH mode; kinetic analysis of MINA sensor; Pt heater power comparison; H_2, acetone, toluene, and formaldehyde sensing performance comparison with previously reported MOX sensors (PDF)

AUTHOR INFORMATION

Corresponding Author

Zhiyong Fan − *Department of Electronic and Computer Engineering, The Hong Kong University of Science and Technology, Kowloon, Hong Kong SAR, China; The Hong Kong University of Science and Technology-Shenzhen Research Institute, Shenzhen 518057, China;* ⓞ orcid.org/0000-0002-5397-0129; Email: eezfan@ust.hk

Authors

Wenying Tang − *Department of Electronic and Computer Engineering, The Hong Kong University of Science and Technology, Kowloon, Hong Kong SAR, China; The Hong Kong University of Science and Technology-Shenzhen Research Institute, Shenzhen 518057, China;* ⓞ orcid.org/0000-0002-7456-9449

Zhesi Chen − *Department of Electronic and Computer Engineering, The Hong Kong University of Science and Technology, Kowloon, Hong Kong SAR, China; The Hong Kong University of Science and Technology-Shenzhen Research Institute, Shenzhen 518057, China*

Zhilong Song − *Department of Electronic and Computer Engineering, The Hong Kong University of Science and Technology, Kowloon, Hong Kong SAR, China; The Hong Kong University of Science and Technology-Shenzhen Research Institute, Shenzhen 518057, China*

Chen Wang − *Department of Electronic and Computer Engineering, The Hong Kong University of Science and Technology, Kowloon, Hong Kong SAR, China; The Hong Kong University of Science and Technology-Shenzhen Research Institute, Shenzhen 518057, China;* ⓞ orcid.org/0000-0002-5678-5287

Zhu'an Wan − *Department of Electronic and Computer Engineering, The Hong Kong University of Science and Technology, Kowloon, Hong Kong SAR, China; The Hong Kong University of Science and Technology-Shenzhen Research Institute, Shenzhen 518057, China*

Chak Lam Jonathan Chan − *Department of Electronic and Computer Engineering, The Hong Kong University of Science and Technology, Kowloon, Hong Kong SAR, China; The Hong Kong University of Science and Technology-Shenzhen Research Institute, Shenzhen 518057, China*

Zhuo Chen − *Department of Electronic and Computer Engineering, The Hong Kong University of Science and Technology, Kowloon, Hong Kong SAR, China; The Hong Kong University of Science and Technology-Shenzhen Research Institute, Shenzhen 518057, China*

Wenhao Ye − *Department of Electronic and Computer Engineering, The Hong Kong University of Science and Technology, Kowloon, Hong Kong SAR, China; The Hong Kong University of Science and Technology-Shenzhen Research Institute, Shenzhen 518057, China*

Complete contact information is available at:
https://pubs.acs.org/10.1021/acsnano.2c03372

Author Contributions

[§]W.T. and Z.C. contributed equally to the work. Z.F., W.T., and Z.C. conceived and designed the experiments. W.T., Z.C., and Z.S. performed the device fabrication and characterization. J.C., Z.W., and W.Y. helped with the gas sensing system setup. Z.C. contributed to the feature extraction and gas discrimination algorithms. Z.W. helped with the TEM characterization and result discussions. Z.S., Z.C., and C.W. helped with the gas-sensing testing and analysis. W.T., Z.C., and Z.F. wrote the manuscript. All authors contributed to result discussions and manuscript revisions.

Notes

The authors declare no competing financial interest.

Fabrication Facility (NFF), the Electronic Packaging Laboratory (EPACK), the Center for 1*D*/2*D* Quantum Materials and the State Key Laboratory on Advanced Displays and Optoelectronics at HKUST, and the MNT Micro and Nanotech Co., LTD at Wuxi, Jiangsu, China.

REFERENCES

(1) Hansen, E. R. The Use of Carbon-Monoxide and Other Gases for Process-Control. *IEEE Trans. Ind. Appl.* **1986**, *22*, 338−344.

(2) Marchisio, A.; Tulliani, J.-M. Semiconducting Metal Oxides Nanocomposites for Enhanced Detection of Explosive Vapors. *Ceramics* **2018**, *1*, 98−119.

(3) Pan, X.; Zhao, X.; Chen, J.; Bermak, A.; Fan, Z. A Fast-Response/Recovery ZnO Hierarchical Nanostructure Based Gas Sensor with Ultra-High Room-Temperature Output Response. *Sens. Actuators, B* **2015**, *206*, 764−771.

(4) Pan, X. F.; Liu, X.; Bermak, A.; Fan, Z. Y. Self-Gating Effect Induced Large Performance Improvement of ZnO Nanocomb Gas Sensors. *ACS Nano* **2013**, *7*, 9318−9324.

(5) Wang, X.; Feng, H. H.; Chen, T.; Zhao, S.; Zhang, J.; Zhang, X. S. Gas Sensor Technologies and Mathematical Modelling for Quality Sensing in Fruit and Vegetable Cold Chains: A Review. *Trends Food Sci. Technol.* **2021**, *110*, 483−492.

(6) Wang, Y.; Huang, J. Recent Advancements in Flexible Humidity Sensors. *J. Semicond.* **2020**, *41*, 040401.

(7) Yan, Q.; Gao, L.; Tang, J.; Liu, H. Flexible and Stretchable Photodetectors and Gas Sensors for Wearable Healthcare Based on Solution-Processable Metal Chalcogenides. *J. Semicond.* **2019**, *40*, 111604.

(8) Yuan, S.; Zhang, S. Recent Progress on Gas Sensors Based on Graphene-like 2D/2D Nanocomposites. *J. Semicond.* **2019**, *40*, 111608.

(9) Galstyan, V.; Bhandari, M. P.; Sberveglieri, V.; Sberveglieri, G.; Comini, E. Metal Oxide Nanostructures in Food Applications: Quality Control and Packaging. *Chemosensors* **2018**, *6*, 16.

(10) Dey, A. Semiconductor Metal Oxide Gas Sensors: A Review. *Mater. Sci. Eng., B* **2018**, *229*, 206−217.

(11) Jeong, S. Y.; Kim, J. S.; Lee, J. H. Rational Design of Semiconductor-Based Chemiresistors and Their Libraries for Next-Generation Artificial Olfaction. *Adv. Mater.* **2020**, *32*, 2002075.

(12) Kolmakov, A.; Klenov, D. O.; Lilach, Y.; Stemmer, S.; Moskovits, M. Enhanced Gas Sensing by Individual SnO₂ Nanowires and Nanobelts Functionalized with Pd Catalyst Particles. *Nano Lett.* **2005**, *5*, 667−673.

(13) Ren, Y.; Zou, Y.; Liu, Y.; Zhou, X.; Ma, J.; Zhao, D.; Wei, G.; Ai, Y.; Xi, S.; Deng, Y. Synthesis of Orthogonally Assembled 3D Cross-Stacked Metal Oxide Semiconducting Nanowires. *Nat. Mater.* **2020**, *19*, 203−211.

(14) Franke, M. E.; Koplin, T. J.; Simon, U. Metal and Metal Oxide Nanoparticles in Chemiresistors: Does the Nanoscale Matter? *Small* **2006**, *2*, 36−50.

(15) Zhang, J.; Liu, X. H.; Neri, G.; Pinna, N. Nanostructured Materials for Room-Temperature Gas Sensors. *Adv. Mater.* **2016**, *28*, 795−831.

(16) Wang, B. H.; Thukral, A.; Xie, Z. Q.; Liu, L. M.; Zhang, X. N.; Huang, W.; Yu, X. G.; Yu, C. J.; Marks, T. J.; Facchetti, A. Flexible and Stretchable Metal Oxide Nanofiber Networks for Multimodal and Monolithically Integrated Wearable Electronics. *Nat. Commun.* **2020**, *11*, 2405.

(17) Kim, H. R.; Haensch, A.; Kim, I. D.; Barsan, N.; Weimar, U.; Lee, J. H. The Role of NiO Doping in Reducing the Impact of Humidity on the Performance of SnO₂-Based Gas Sensors: Synthesis Strategies, and Phenomenological and Spectroscopic Studies. *Adv. Funct. Mater.* **2011**, *21*, 4456−4463.

(18) Fan, Z. Y.; Lu, J. G. Gate-Refreshable Nanowire Chemical Sensors. *Appl. Phys. Lett.* **2005**, *86*, 123510.

(19) Fan, Z. Y.; Wang, D. W.; Chang, P. C.; Tseng, W. Y.; Lu, J. G. ZnO Nanowire Field-Effect Transistor and Oxygen Sensing Property. *Appl. Phys. Lett.* **2004**, *85*, 5923−5925.

(20) Yao, M. S.; Tang, W. X.; Wang, G. E.; Nath, B.; Xu, G. MOF Thin Film-Coated Metal Oxide Nanowire Array: Significantly Improved Chemiresistor Sensor Performance. *Adv. Mater.* **2016**, *28*, 5229−5234.

(21) Moon, Y. K.; Jeong, S. Y.; Kang, Y. C.; Lee, J. H. Metal Oxide Gas Sensors with Au Nanocluster Catalytic Overlayer: Toward Tuning Gas Selectivity and Response Using a Novel Bilayer Sensor Design. *ACS Appl. Mater. Interfaces.* **2019**, *11*, 32169−32177.

(22) Singh, A.; Sikarwar, S.; Verma, A.; Yadav, B. C. The Recent Development of Metal Oxide Heterostructures Based Gas Sensor, Their Future Opportunities and Challenges: A Review. *Sens. Actuators, A* **2021**, *332*, 113127.

(23) Song, Z. L.; Ye, W. H.; Chen, Z.; Chen, Z. S.; Li, M. T.; Tang, W. Y.; Wang, C.; Wan, Z. A.; Poddar, S.; Wen, X. L.; et al. Wireless Self-Powered High-Performance Integrated Nanostructured-Gas-Sensor Network for Future Smart Homes. *ACS Nano* **2021**, *15*, 7659−7667.

(24) Chen, J. Q.; Chen, Z.; Boussaid, F.; Zhang, D. Q.; Pan, X. F.; Zhao, H. J.; Bermak, A.; Tsui, C. Y.; Wang, X. R.; Fan, Z. Y. Ultra-Low-Power Smart Electronic Nose System Based on Three-Dimensional Tin Oxide Nanotube Arrays. *ACS Nano* **2018**, *12*, 6079−6088.

(25) Chen, Z.; Chen, Z.; Song, Z.; Ye, W.; Fan, Z. Smart Gas Sensor Arrays Powered by Artificial Intelligence. *J. Semicond.* **2019**, *40*, 111601.

(26) Van den Broek, J.; Abegg, S.; Pratsinis, S. E.; Guntner, A. T. Highly Selective Detection of Methanol over Ethanol by a Handheld Gas Sensor. *Nat. Commun.* **2019**, *10*, 4220.

(27) Potyrailo, R. A.; Go, S.; Sexton, D.; Lie, X. X.; Alkadi, N.; Kolmakov, A.; Amm, B.; St-Pierre, R.; Scherer, B.; Nayeri, M.; et al. Extraordinary Performance of Semiconducting Metal Oxide Gas Sensors Using Dielectric Excitation. *Nat. Electron.* **2020**, *3*, 280−289.

(28) Liu, H. Y.; He, Y. H.; Nagashima, K.; Meng, G.; Dai, T. T.; Tong, B.; Deng, Z. H.; Wang, S. M.; Zhu, N. W.; Yanagida, T.; et al. Discrimination of VOCs Molecules via Extracting Concealed Features from a Temperature-Modulated P-type NiO Sensor. *Sens. Actuators, B* **2019**, *293*, 342−349.

(29) Djedidi, O.; Djeziri, M. A.; Morati, N.; Seguin, J. L.; Bendahan, M.; Contaret, T. Accurate Detection and Discrimination of Pollutant Gases Using a Temperature Modulated MOX Sensor Combined with Feature Extraction and Support Vector Classification. *Sens. Actuators, B* **2021**, *339*, 129817.

(30) Kanaparthi, S.; Singh, S. G. Discrimination of Gases with A Single Chemiresistive Multi-Gas Sensor Using Temperature Sweeping and Machine Learning. *Sens. Actuators, B* **2021**, *348*, 130725.

(31) Iwata, T.; Saeki, M.; Okura, Y.; Yoshikawa, T. Gas Discrimination Based on Enhanced Gas-Species Related Information Obtained by A Single Gas Sensor with Novel Temperature Modulation. *Sens. Actuators, B* **2022**, *354*, 131225.

(32) Suematsu, K.; Harano, W.; Oyama, T.; Shin, Y.; Watanabe, K.; Shimanoe, K. Pulse-Driven Semiconductor Gas Sensors Toward ppt Level Toluene Detection. *Anal. Chem.* **2018**, *90*, 11219−11223.

(33) Liang, X.; Kim, T. H.; Yoon, J. W.; Kwak, C. H.; Lee, J. H. Ultrasensitive and Ultraselective Detection of H₂S Using Electrospun CuO-loaded In₂O₃ Nanofiber Sensors Assisted by Pulse Heating. *Sens. Actuators, B* **2015**, *209*, 934−942.

(34) Suematsu, K.; Oyama, T.; Mizukami, W.; Hiroyama, Y.; Watanabe, K.; Shimanoe, K. Selective Detection of Toluene Using Pulse-Driven SnO₂ Micro Gas Sensors. *ACS Appl. Electron. Mater.* **2020**, *2*, 2913−2920.

(35) Suematsu, K.; Hiroyama, Y.; Harano, W.; Mizukami, W.; Watanabe, K.; Shimanoe, K. Double-Step Modulation of the Pulse-Driven Mode for a High-Performance SnO₂ Micro Gas Sensor: Designing the Particle Surface via a Rapid Preheating Process. *ACS Sens* **2020**, *5*, 3449−3456.

(36) Suh, J. H.; Cho, I.; Kang, K.; Kweon, S. J.; Lee, M.; Yoo, H. J.; Park, I. Fully Integrated and Portable Semiconductor-Type Multi-Gas

Sensing Module for IoT Applications. *Sens. Actuators, B* **2018**, *265*, 660−667.

(37) Dai, T. T.; Meng, G.; Deng, Z. H.; Chen, Y.; Liu, H. Y.; Li, L.; Wang, S. M.; Chang, J. Q.; Xu, P. C.; Li, X. X.; et al. Generic Approach to Boost the Sensitivity of Metal Oxide Sensors by Decoupling the Surface Charge Exchange and Resistance Reading Process. *ACS Appl. Mater. Interfaces.* **2020**, *12*, 37295−37304.

(38) Xu, L.; Dai, Z. F.; Duan, G. T.; Guo, L. F.; Wang, Y.; Zhou, H.; Liu, Y. X.; Cai, W. P.; Wang, Y. L.; Li, T. Micro/Nano Gas Sensors: A New Strategy Towards In-Situ Wafer-Level Fabrication of High-Performance Gas Sensing Chips. *Sci. Rep.* **2015**, *5*, 10507.

(39) Hwang, I. S.; Lee, E. B.; Kim, S. J.; Choi, J. K.; Cha, J. H.; Lee, H. J.; Ju, B. K.; Lee, J. H. Gas Sensing Properties of SnO$_2$ Nanowires on Micro-Heater. *Sens. Actuators, B* **2011**, *154*, 295−300.

(40) Rao, A.; Long, H.; Harley-Trochimczyk, A.; Pham, T.; Zettl, A.; Carraro, C.; Maboudian, R. In Situ Localized Growth of Ordered Metal Oxide Hollow Sphere Array on Microheater Platform for Sensitive, Ultra-Fast Gas Sensing. *ACS Appl. Mater. Interfaces.* **2017**, *9*, 2634−2641.

(41) Kwak, S.; Shim, Y.-S.; Yoo, Y. K.; Lee, J.-H.; Kim, I.; Kim, J.; Lee, K. H.; Lee, J. H. MEMS-Based Gas Sensor Using PdO-Decorated TiO$_2$ Thin Film for Highly Sensitive and Selective H$_2$ Detection with Low Power Consumption. *Electron. Mater. Lett.* **2018**, *14*, 305−313.

(42) Cho, I.; Kang, K.; Yang, D.; Yun, J.; Park, I. Localized Liquid-Phase Synthesis of Porous SnO$_2$ Nanotubes on MEMS Platform for Low-Power, High Performance Gas Sensors. *ACS Appl. Mater. Interfaces.* **2017**, *9*, 27111−27119.

(43) Choi, K. W.; Lee, J. S.; Seo, M. H.; Jo, M. S.; Yoo, J. Y.; Sim, G. S.; Yoon, J. B. Batch-Fabricated CO Gas Sensor in Large-Area (8-in.) with Sub-10 mW Power Operation. *Sens. Actuators, B* **2019**, *289*, 153−159.

(44) Long, H.; Harley-Trochimczyk, A.; He, T. Y.; Pham, T.; Tang, Z. R.; Sho, T. L.; Zettl, A.; Mickelson, W.; Carraro, C.; Maboudian, R. In Situ Localized Growth of Porous Tin Oxide Films on Low Power Microheater Platform for Low Temperature CO Detection. *ACS Sens* **2016**, *1*, 339−343.

(45) Rojo, M. M.; Martin, J.; Grauby, S.; Borca-Tasciuc, T.; Dilhaire, S.; Martin-Gonzalez, M. Decrease in Thermal Conductivity in Polymeric P3HT Nanowires by Size-Reduction Induced by Crystal Orientation: New Approaches Towards Thermal Transport Engineering of Organic Materials. *Nanoscale* **2014**, *6*, 7858−7865.

(46) Aragon, F. H.; Coaquira, J. A. H.; Gonzalez, I.; Nagamine, L. C. C. M.; Macedo, W. A. A.; Morais, P. C. Fe Doping Effect on the Structural, Magnetic and Surface Properties of SnO$_2$ Nanoparticles Prepared by a Polymer Precursor Method. *J. Phys. D: Appl. Phys.* **2016**, *49*, 155002.

(47) Aragon, F. H.; Gonzalez, I.; Coaquira, J. A. H.; Hidalgo, P.; Brito, H. F.; Ardisson, J. D.; Macedo, W. A. A.; Morais, P. C. Structural and Surface Study of Praseodymium-Doped SnO$_2$ Nanoparticles Prepared by the Polymeric Precursor Method. *J. Phys. Chem. C* **2015**, *119*, 8711−8717.

(48) Li, G. J.; Wang, X. H.; Yan, L. M.; Wang, Y.; Zhang, Z. Y.; Xu, J. Q. PdPt Bimetal-Functionalized SnO$_2$ Nanosheets: Controllable Synthesis and Its Dual Selectivity for Detection of Carbon Monoxide and Methane. *ACS Appl. Mater. Interfaces.* **2019**, *11*, 26116−26126.

(49) Militello, M. C.; Simko, S. J. Palladium Chloride (PdCl$_2$) by XPS. *Surf. Sci. Spectra.* **1994**, *3*, 402−409.

(50) Wang, X. B.; Wang, Y. Y.; Tian, F.; Liang, H. J.; Wang, K.; Zhao, X. H.; Lu, Z. S.; Jiang, K.; Yang, L.; Lou, X. D. From the Surface Reaction Control to Gas-Diffusion Control: The Synthesis of Hierarchical Porous SnO$_2$ Microspheres and Their Gas-Sensing Mechanism. *J. Phys. Chem. C* **2015**, *119*, 15963−15976.

(51) Chang, C.-M.; Hon, M.-H.; Leu, I.-C. Improvement in CO Sensing Characteristics by Decorating ZnO Nanorod Arrays with Pd Nanoparticles and the Related Mechanisms. *RSC Adv.* **2012**, *2*, 2469−2475.

(52) DiGiulio, M.; Micocci, G.; Serra, A.; Tepore, A.; Rella, R.; Siciliano, R. Characteristics of Reactively Sputtered Pt-SnO$_2$ Thin Films for CO Gas Sensors. *J. Vac Sci. Technol. A* **1996**, *14*, 2215−2219.

(53) Yamazoe, N.; Shimanoe, K. Fundamentals of Semiconductor Gas Sensors. *Semiconductor Gas Sensors*, 2nd ed.; Woodhead Publishing: Cambridge, United Kingdom, 2020; pp 3−38.

(54) Gao, J.; Teplyakov, A. V. Chemical Transformations of Acetone on ZnO Powder. *J. Catal.* **2014**, *319*, 136−141.

(55) Shao, C. J.; Chang, Y. Q.; Long, Y. High Performance of Nanostructured ZnO Film Gas Sensor at Room Temperature. *Sens. Actuators, B* **2014**, *204*, 666−672.

(56) Chen, J.; Pan, X.; Boussaid, F.; McKinley, A.; Fan, Z.; Bermak, A. Breath Level Acetone Discrimination Through Temperature Modulation of a Hierarchical ZnO Gas Sensor. *IEEE Sensors Letters* **2017**, *1*, 1−4.

(57) Jolliffe, I. T.; Cadima, J. Principal Component Analysis: A Review and Recent Developments. *Philos. T R Soc. A* **2016**, *374*, 20150202.

(58) Ding, J. H.; McAvoy, T. J.; Cavicchi, R. E.; Semancik, S. Surface State Trapping Models for SnO$_2$-based Microhotplate Sensors. *Sens. Actuators, B* **2001**, *77*, 597−613.

(59) Baur, T.; Schutze, A.; Sauerwald, T. Optimization of Temperature Cycled Operation of Semiconductor Gas Sensors. *Tm-Tech Mess.* **2015**, *82*, 187−195.

(60) Schultealbert, C.; Baur, T.; Schutze, A.; Bottcher, S.; Sauerwald, T. A Novel Approach Towards Calibrated Measurement of Trace Gases Using Metal Oxide Semiconductor Sensors. *Sens. Actuators, B* **2017**, *239*, 390−396.

(61) Sakai, G.; Matsunaga, N.; Shimanoe, K.; Yamazoe, N. Theory of Gas-Diffusion Controlled Sensitivity for Thin Film Semiconductor Gas Sensor. *Sens. Actuators, B* **2001**, *80*, 125−131.

(62) Jones, D. R.; Maffeis, T. G. G. Analysis of the Kinetics of Surface Reactions on a Zinc Oxide Nanosheet-Based Carbon Monoxide Sensor Using an Eley-Rideal Model. *Sens. Actuators, B* **2015**, *218*, 16−24.

(63) Weinberg, W. H. Eley-Rideal Surface Chemistry: Direct Reactivity of Gas Phase Atomic Hydrogen with Adsorbed Species. *Acc. Chem. Res.* **1996**, *29*, 479−487.

(64) Acharyya, S.; Nag, S.; Kimbahune, S.; Ghose, A.; Pal, A.; Guha, P. K. Selective Discrimination of VOCs Applying Gas Sensing Kinetic Analysis over a Metal Oxide-Based Chemiresistive Gas Sensor. *ACS Sens* **2021**, *6*, 2218−2224.

(65) Suematsu, K.; Shin, Y.; Hua, Z. Q.; Yoshida, K.; Yuasa, M.; Kida, T.; Shimanoe, K. Nanoparticle Cluster Gas Sensor: Controlled Clustering of SnO$_2$ Nanoparticles for Highly Sensitive Toluene Detection. *ACS Appl. Mater. Interfaces.* **2014**, *6*, 5319−5326.

(66) Hu, H.; Trejo, M.; Nicho, M. E.; Saniger, J. M.; Garcia-Valenzuela, A. Adsorption Kinetics of Optochemical NH$_3$ Gas Sensing with Semiconductor Polyaniline Films. *Sens. Actuators, B* **2002**, *82*, 14−23.

(67) Vuong, N. M.; Kim, D.; Kim, H. Surface Gas Sensing Kinetics of a WO$_3$ Nanowire Sensor: Part 2-Reducing Gases. *Sens. Actuators, B* **2016**, *224*, 425−433.

(68) Fort, A.; Mugnaini, M.; Rocchi, S.; Serrano-Santos, M. B.; Vignoli, V.; Spinicci, R. Simplified Models for SnO$_2$ Sensors During Chemical and Thermal Transients in Mixtures of Inert, Oxidizing and Reducing Gases. *Sens. Actuators, B* **2007**, *124*, 245−259.

(69) Borman, P.; Elder, D. Q2 (R1) Validation of Analytical Procedures. *ICH Quality Guidelines: An Implementation Guide*; John Wiley & Sons: Hoboken, NJ, 2017; Vol. *5*, pp 127−166.